Redox Biology 92 (2026) 104147

Contents lists available at ScienceDirect

Redox Biology

journal homepage: www.elsevier.com/locate/redox

# An improved fluorescent indicator for monitoring intracellular redox potential

Zhengcai Ma [a,b,1], Jianbin Cao [c,1], Hongxiang Zeng [d,1], Jiahuan Zhu [e,1], Runchun Li [h], Xueling Wang [h], Cun Yin [b], Lingyang Chen [c], Bing Liu [f], Rong Shen [g], Mingcang Wang [c], Wengang Li [h], Jingxun Wu [i,*], Dan Du [b,j,k,**], Rongkun Tao [b,***]

[a] *Faculty of Chemistry and Life Sciences, Gansu Minzu Normal University, Gansu, 747000, China*
[b] *Clinical Research Institute, The First Affiliated Hospital of Xiamen University, School of Medicine, Xiamen University, Fujian, 361102, China*
[c] *Department of Anesthesiology, Taizhou Hospital of Zhejiang Province Affiliated to Wenzhou Medical University, Zhejiang, 317000, China*
[d] *State Key Laboratory of Quantitative Synthetic Biology, Shenzhen Institute of Synthetic Biology, Shenzhen Institutes of Advanced Technology, Chinese Academy of Sciences, Shenzhen, 518055, China*
[e] *Synthetic Biology and Biotechnology Laboratory, State Key Laboratory of Bioreactor Engineering, Shanghai Collaborative Innovation Center for Biomanufacturing Technology, East China University of Science and Technology, 130 Mei Long Road, Shanghai, 200237, China*
[f] *Zhejiang Key Laboratory of Medical Epigenetics, Department of Biochemistry and Molecular Biology, School of Basic Medical Sciences, Hangzhou Normal University, Hangzhou, 311121, China*
[g] *Clinical Research Institute, School of Medicine, Xiamen University, Fujian, 361102, China*
[h] *Department of Hepatobiliary Surgery, Xiang'an Hospital of Xiamen University, Cancer Research Center, School of Medicine, Xiamen University, Xiamen, Fujian, 361102, China*
[i] *Department of Medical Oncology, The First Affiliated Hospital of Xiamen University, School of Medicine, Xiamen University, Xiamen, Fujian, 361102, China*
[j] *State Key Laboratory of Cellular Stress Biology, Department of Gastroenterology, School of Medicine, Faculty of Medicine and Life Sciences, Xiamen University, Fujian, 361102, China*
[k] *Cancer Research Center, Department of Stomatology, School of Medicine, Xiamen University, Fujian, 361102, China*

A R T I C L E I N F O

*Keywords:*
Redox potential
roGFP
Zebrafish

A B S T R A C T

The intracellular redox balance, which is determined by the relative levels of oxidants and reductants, plays a crucial role in regulating various cellular processes. Genetically encoded redox-sensitive green fluorescent proteins (roGFPs) are invaluable tools for spatiotemporally monitoring intracellular redox potential. However, the relatively low fluorescence intensity and weak response of existing sensors have restricted their applications in subcellular organelles, such as the Golgi apparatus, and in living animals. In this study, we rationally engineered an enhanced roGFP variant (eroGFP1.2), which exhibited a more than fivefold increase in fluorescence brightness and a 50% greater dynamic range compared to the wild-type roGFP1 in both *E. coli* and HeLa cells. Using the eroGFP1.2 sensor, we calibrated redox potential across different subcellular compartments within HeLa cells. Furthermore, when fused to human glutaredoxin-1 (Grx1), the chimeric sensor enabled specific and sensitive detection of glutathione redox dynamics in living cells. We also employed eroGFP1.2 to monitor a reactive oxygen species (ROS) burst at the wound site following tailfin transection in larval zebrafish. This work advances our understanding of GFP-based biosensor optimization and provides a powerful, high-sensitivity tool for investigating thiol-disulfide redox regulation in live cells and intact organisms.

* Corresponding author.
** Corresponding author. Clinical Research Institute, The First Affiliated Hospital of Xiamen University, School of Medicine, Xiamen University, Fujian, 361102, China.
*** Corresponding author.
*E-mail addresses:* wujingxun@xmu.edu.cn (J. Wu), dandu@xmu.edu.cn (D. Du), taorongkun@xmu.edu.cn (R. Tao).
[1] These authors contributed equally.

https://doi.org/10.1016/j.redox.2026.104147
Received 6 February 2026; Received in revised form 26 March 2026; Accepted 28 March 2026
Available online 30 March 2026

## 1. Introduction

Redox homeostasis is tightly regulated to support a wide range of essential cellular functions, including cell signaling, mitosis, immune response, cell death, and metabolism [1–6]. This sophisticated control system maintains an appropriate balance between oxidants and reductants (the redox poise) within distinct subcellular compartments, which is critical for their specific functions. For instance, the cytosol and mitochondria exhibit a relatively reduced environment, characterized by a high reduced glutathione/oxidized glutathione (GSH/GSSG) ratio. This protects cysteine residues in proteins from oxidative damage and supports reductive biochemical reactions [7,8]. Conversely, the endoplasmic reticulum (ER) maintains a more oxidized redox potential, essential for the correct formation of disulfide bonds during the folding of secreted and membrane proteins [9]. This compartmentalization underscores the importance of accurately measuring redox potential differences across organelles to understand their unique physiological and pathological roles [10–12].

Genetically encoded redox-sensitive green fluorescent proteins (roGFPs) provide a powerful non-invasive method for spatially and temporally resolving intracellular redox status [13]. Their function is based on a conformational change induced by disulfide formation (or reduction) between two engineered cysteine residues (C147 and C204) located on adjacent β-strands of the β-barrel structure in GFP. The dynamics of the disulfide bond alter the chromophore's protonation state, causing a measurable shift in its excitation spectrum [14]. By targeting roGFPs to specific organelles, it becomes possible to quantify redox potential based on excitation ratio measurements [15]. However, detecting redox potential dynamics within subcellular organelles and *in vivo* remains a significant challenge, primarily due to the low fluorescence intensity and limited dynamic range of currently available roGFP sensors.

In this study, we rationally engineered a bright and highly responsive redox-sensitive biosensor, eroGFP1.2, by incorporating reported mutations from Superfolder GFP (sfGFP; namely S30R, S39R, N105T, I171V, A206V) and pHluorin3 (L220F) into the roGFP1 scaffold via targeted mutagenesis [16,17]. We demonstrated that eroGFP1.2 is effective in monitoring redox equilibrium dynamics in *Escherichia coli (E. coli)* and in calibrating compartment-specific redox potentials in HeLa cells. We also engineered a Grx1-eroGFP1.2 fusion construct that functions as a selective biosensor for detecting dynamic changes in the intracellular glutathione redox state. Furthermore, we showed that eroGFP1.2 enables visualization of ROS bursts at zebrafish wound sites, mediated by NADPH oxidase activity.

## 2. Results

### 2.1. Rational design enhanced roGFP mutants

To improve the properties of roGFP, we drew inspiration from the development of Superfolder GFP (sfGFP) [16] and the optimization of GFP-based pHluroin sensors [18–21]. The mutation sites used to create sfGFP are common among various GFP-based fluorescent protein palettes, such as sfBFP, sfCFP and sfYFP [16]. These mutations can reduce folding hindrance in roGFP and accelerate chromophore formation [16]. For the GFP-based pH sensor, pHluorin is a pH-responsive indicator with similar structure to roGFPs. Several enhanced pHluorin variants, such as pHluorin2 [18], iR-pHluorin [20,21] and pHluorin3 [17], have demonstrated increased fluorescence intensity and a stronger response, providing valuable insights for optimizing roGFP [21].

We hypothesized that the mutations F46L and M153T, derived from iR-pHluorin [20], might also be effective on roGFP1 (Supplementary Fig. 1A). We introduced the two mutations into roGFP by site-specific mutagenesis, and the resulting plasmids were transformed into BL21 (DE3), where they were subjected to a redox challenge. However, both mutations failed to enhance either fluorescence intensity or response (Supplementary Fig. 1B and 1C).

Based on the rationale that the L220F mutation in pHluorin3 enhances its pH response, we introduced this single mutation into roGFP1 (Fig. 1A). Subsequent measurement of fluorescence in bacterial suspensions revealed that the L220F variant led to a 1.6-fold increase in the maximal response; however, fluorescence intensity was reduced by half when compared to the parent roGFP1 (Fig. 1B and C). This mutant was designated enhanced roGFP (eroGFP1.0, Supplementary Table 1). We hypothesized that the large aromatic amino acid might interact with the chromophore to amplify the response but also impair protein folding.

To improve the folding ability of eroGFP1.0, we sequentially introduced substitutions described in sfGFP (S30R, S39R, N105T, Y145F, I171V, A206V) into eroGFP1.0 (Fig. 1A, Supplementary Fig. 1D and Supplementary Table 1). This led to the creation of two novel bright sensors: eroGFP1.1 (incorporating all six sfGFP-specific mutations) and eroGFP1.2 (which omits the Y145F mutation present in eroGFP1.1). Both mutants displayed significantly enhanced baseline fluorescence, approximately 3.5-fold and 5-fold higher baseline fluorescence versus roGFP1, respectively (Fig. 1B and D and Supplementary Note 1, 2). Moreover, the maximal response was increased by about 50% relative to roGFP1 expressed in bacteria (Fig. 1C and Supplementary Fig. 1G). Additionally, compared to roGFP2, eroGFP1.2 exhibited a similar fluorescence level at 488 nm excitation and an ~8-fold greater intensity at 400 nm excitation (Supplementary Fig. 1E–F). Western blot analysis revealed similar total protein levels across the roGFP variants (Supplementary Fig. 1H and 1I), confirming that the enhanced fluorescence of eroGFP1.2 arises from improved folding efficiency mediated by the introduced Superfolder mutations.

To determine whether this approach could be applied to other roGFP variants, we introduced the same mutations into roGFP2. However, roGFP2-L220F showed a decrease in both fluorescence intensity and response (Supplementary Fig. 1J and 1K). As expected, incorporating the Superfolder substitutions to roGFP2 dramatically increased its fluorescence, resulting in eroGFP2.2 (Fig. 1E). Additionally, the Y145F mutation, which reduces polarity, impaired chromophore maturation and consequently decreased fluorescence, similar to what was observed in eroGFP1.1.

### 2.2. In vitro characterization of eroGFP

The eroGFP sensor proteins were purified using NTA affinity chromatography and subsequently characterized *in vitro*. The fluorescence spectra of eroGFPs closely resembled that of the parental roGFP1, exhibiting two excitation peaks near 400 nm and 480 nm, with a shared emission peak at approximately 510 nm (Fig. 2A). Upon oxidation, the reduced form of eroGFP showed more than a sixfold decrease in fluorescence at ex480 nm and a ~20% increase in fluorescence at ex400 nm (Fig. 2B and C and Supplementary Table 2). The resulting dynamic range, defined as the maximal fluorescence change of the excitation fluorescence ratio $R_{400/480}$ between the fully oxidized and reduced states (i.e. $R_{400/480ox}/R_{400/480red}$), reached up to ~6.0-fold for eroGFP1.1 and ~6.5-fold for eroGFP1.2 (Fig. 2D and Supplementary Fig. 2A).

Redox titration further revealed midpoint redox potentials of −264 mV for eroGFP1.1 and −266 mV for eroGFP1.2 (Fig. 2E and Supplementary Table 2), which are slightly more oxidizing than that of roGFP1 (−285 mV). Notably, the fluorescence excitation ratios of the eroGFPs remained stable across a broad pH range of 5.5 to 8.5 (Fig. 2F and Supplementary Fig. 2B–D) and less pH sensitivity than roGFP2 (Supplementary Fig. 2E–I), confirming robustness against physiological pH fluctuations.

Given that model organisms can thrive across wide temperature ranges [22–24], we evaluated the temperature dependence of roGFP sensor responses. The maximal changes in the excitation ratios of roGFP sensor ($R_{400/480}$) under oxidation and reduction state remained unchanged between 25 °C and 40 °C (Supplementary Fig. 2J). Remarkably, we observed that the roGFP sensors demonstrated moderate resistance

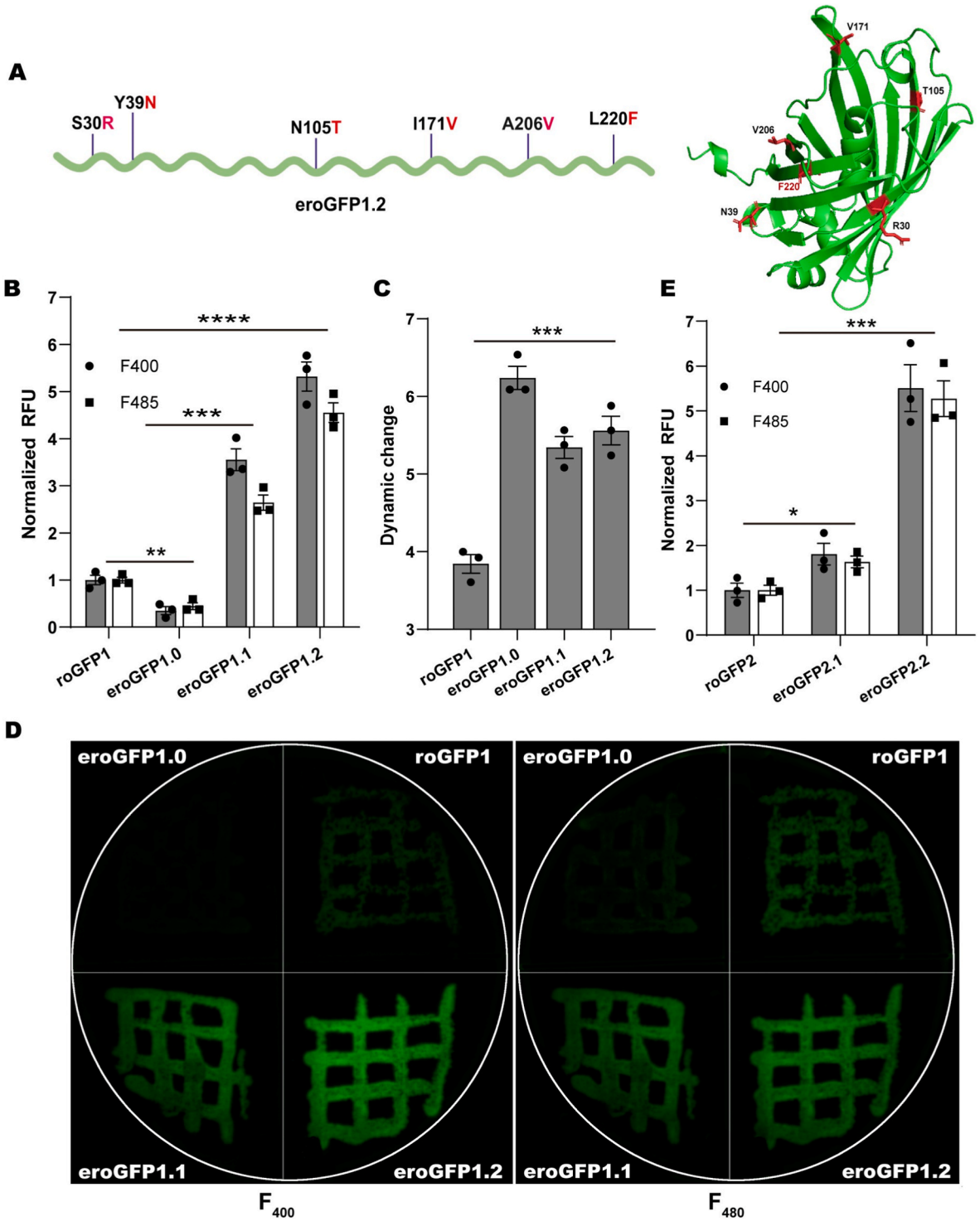


**Fig. 1. Rational design of enhanced roGFP mutants. (A)** Schematic representation of eroGFP1.2. The residues in the wild-type roGFP1 are shown in black, while the mutated residues are highlighted in red. **(B)** The baseline brightness of constructed mutants expressed in *Escherichia coli*. $F_{400}$ and $F_{485}$ are defined as the emission fluorescence intensity captured under excitation at 400 nm and 485 nm, respectively. Both excited channel fluorescence of roGFP1 sensor were normalized to 1.0. **(C)** The dynamic changes were calculated using the excitation ratio of the fully oxidized sensor divided by that of the fully reduced sensor, which were performed by adding 0.1 mM diamide and 5 mM dithiothreitol (DTT) into the bacterial suspensions and monitored by the fluorescence plate reader. **(D)** The representative fluorescence images of roGFP1 and the enhanced variants in bacterial colony on LB plates. All indicators were transfected into *E.coli* and cultured at 37 °C overnight. The images were taken 20 h post-transfection using In-Vivo Multispectral System FX with two excitation filters 400/10 (left) and 480/10 (right) and an emission filter of 530 nm. **(E)** The fluorescence of roGFP2, eroGFP2.1 and eroGFP2.2 expressed in bacteria. The detection conditions are the same in (B). Data are from three independent experiments (n = 3). Error bars indicate standard deviation of the mean. Two-way ANOVA was used for paired comparisons in B, C and E. Unpaired one-tailed Student's *t*-test was used for C. For statistical analysis, *, $P < 0.05$; **, $P < 0.01$; ***, $P < 0.001$; ****, $P < 0.0001$.

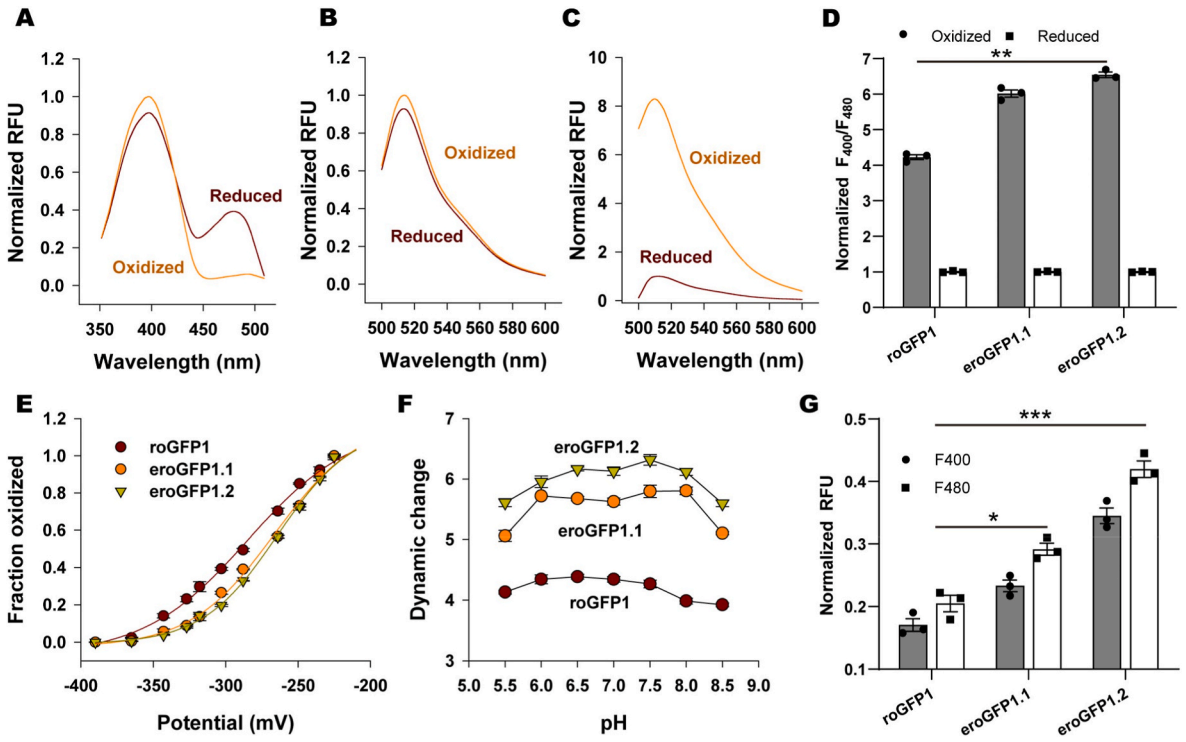


**Fig. 2. Fluorescent properties of eroGFPs. (A–C)** Fluorescence spectra of fully oxidized and reduced eroGFP1.2 in the presence 0.1 mM diamide and 5 mM DTT, respectively. Excitation spectrum has two peaks at 400 nm and 480 nm (A). Emission spectra upon excitation at 400 nm (B) and 480 nm (C). **(D)** Dynamic excitation ratio 400/480 was measured *in vitro* with a fluorescence plate reader. $F_{400}/F_{480}$ of reduced roGFPs was normalized to 1. Data as follows are treated with the same manner if not mentioned. Error bars represent SEM. **(E)** Redox titration were determined by plotting the fraction of oxidized protein versus the equivalent redox potential values. The mid-point redox potential values of the roGFPs were calculated by fitting data. **(F)** The dynamic ranges of roGFP1, eroGFP1.1 and eroGFP1.2 in response to DTT and diamide at different pH values. The buffer contained 100 mM MES (pH 5.5-6.5) or HEPES (pH 7.0-8.0) or TRICINE (pH 8.5), 100 mM sodium chloride. **(G)** The residual dual-channel fluorescence of roGFP sensors after heat treatment at 90 °C for 30 min. Two-way ANOVA was used for paired comparisons in D and G. *, $P < 0.05$; **, $P < 0.01$; ***, $P < 0.001$.

to high temperatures ranging from 60 °C to 90 °C. Under these extreme conditions, eroGFP1.2 retained approximately 40% of its fluorescence signal after 30 min at 90 °C, compared to only ~20% retention by roGFP1 (Fig. 2G, Supplementary Fig. 2K and 2L), indicating improved thermal stability.

We also investigated the impact of chloride ion concentration on sensor performance. The fluorescence emission ratios of eroGFPs remained largely unaffected across varying chloride levels (Supplementary Fig. 2M), suggesting that these sensors can be used into various subcellular organelles [25,26].

Taken together, the improved eroGFP1.2 with enhanced brightness, broad pH insensitivity, thermal resilience, and expanded dynamic range is a powerful tool for accurate and sensitive detection of redox potential in living systems.

### 2.3. Imaging of cytosolic redox changes with eroGFP1.2

To determine whether eroGFP1.2 functions in mammalian cells, we subcloned it into the pcDNA3.1 vector and expressed it in HeLa cells (Fig. 3A). Upon expression, eroGFP1.2 exhibited intense fluorescence throughout the cell cytoplasm (Fig. 3B and Supplementary Fig. 3A). Quantitative analysis showed that eroGFP1.2 fluorescence intensity ($F_{407}$ and $F_{482}$) was higher than roGFP1 and roGFP2 (Fig. 3B and Supplementary Fig. 3A–C). Fluorescence ratio imaging ($F_{407}/F_{482}$) revealed no significant differences in signal between the cytosol and nucleus (Fig. 3C), suggesting similar basal redox potentials in these compartments.

We monitored the baseline fluorescence of eroGFP1.2-positive cells for 3 min (Fig. 3C and D, and Supplementary Fig. 3D and 3E). Upon administration of 0.1 mM diamide, a potent oxidizing agent, the cells exhibited a rapid and robust oxidative response, with the fluorescence ratio increasing approximately 3-fold within 2 min (Fig. 3C and D, and Supplementary Fig. 3D and 3E). Subsequently, treatment with 5 mM dithiothreitol (DTT), a reducing agent, effectively reversed the oxidized sensor back to a reduced state, even lower than the initial baseline state (Fig. 3C and D, and Supplementary Fig. 3D and 3E). The fluorescence response of eroGFP1.2 was larger than roGFP1 and roGFP2, demonstrating the improved dynamic range in mammalian cells (Supplementary Fig. 3F and 3G).

To characterize the cytosolic redox potential with eroGFP1.2, we set the excitation ratios in cell under treatments of reductant (5 mM DTT) and oxidant (0.1 mM diamide) as the minimum and maximum ratios *in situ*, respectively (Fig. 3E and Supplementary Fig. 3F). We found that the oxidation fraction of cytosolic sensor was ~8.3% in physiological HeLa cells (Fig. 3F), implying a basal redox potential of −328 mV after fitting to the *in vitro* calibration curve (Fig. 3G), consistent with previously reported value in mammalian cells [14].

These findings demonstrate that eroGFP1.2 functions effectively in living mammalian cells, enabling dynamic, reversible monitoring of intracellular redox changes. Its enhanced fluorescence intensity and quantitative response make it a valuable tool for real-time redox potential calibration and imaging *in situ*.

### 2.4. Calibration redox potential in compartments of HeLa cells

We next investigated whether the enhanced eroGFP1.2 enables detection of redox potential within specific subcellular compartments of mammalian cells. We targeted eroGFP1.2 to multiple organelles using validated localization signals for the mitochondrial matrix, plasma membrane (PM), golgi apparatus (Gol) and endoplasmic reticulum (ER)

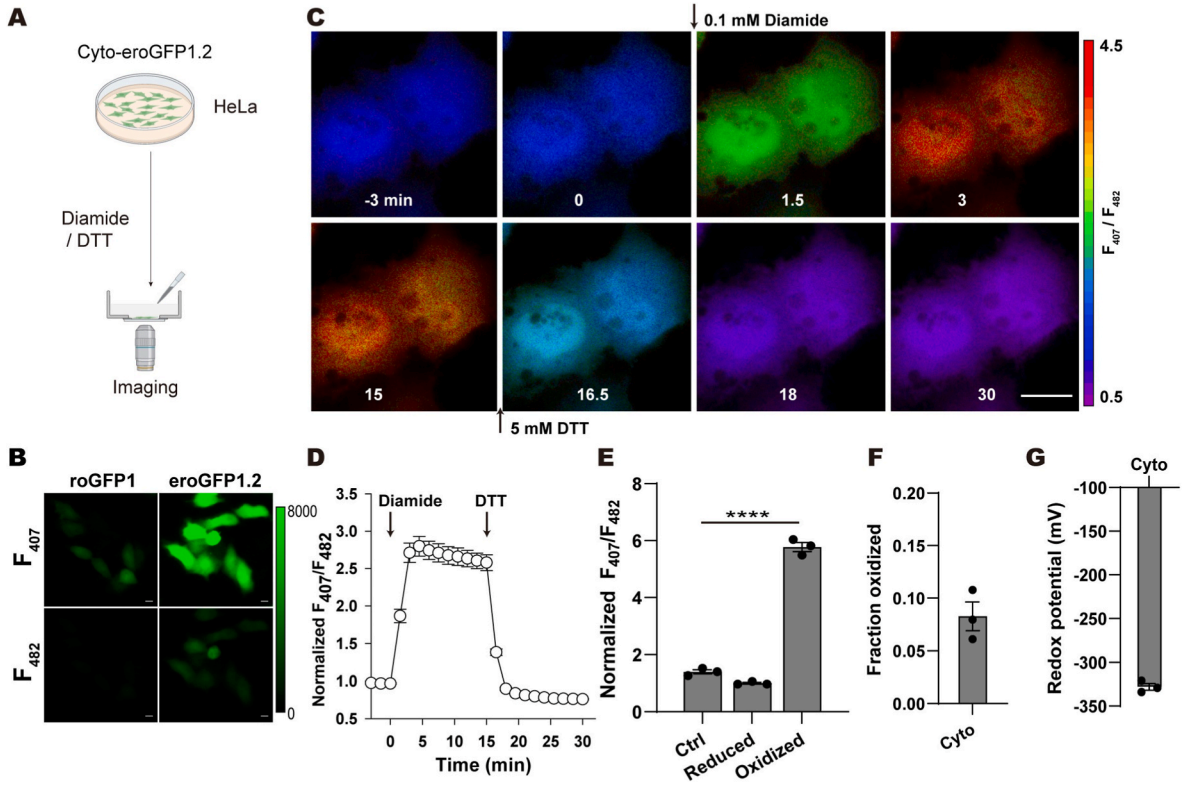


**Fig. 3. Monitoring of cytoplasmic redox dynamics of HeLa cells. (A)** Schematic of the detection of cytosolic eroGFP sensor in HeLa cells by imaging. **(B)** The representative images of HeLa cells expressing roGFP1 (left) and eroGFP1.2 (right). **(C)** HeLa cells expressing eroGFP1.2 were treated with 0.1 mM diamide at 0 min, followed by addition of 5 mM DTT 15 min later. Pseudocolored ratio images of the cells at indicated time points exemplify the response kinetic of eroGFP1.2. **(D)** In this experiment, the time course of excitation ratios of eroGFP1.2 was averaged and plotted using ten individual cells. The addition of diamide and DTT were indicated by arrows. **(E)** The normalized $F_{407}/F_{482}$ of eroGFP1.2 sensor in cells without perturbance (Ctrl), under DTT treatment (Reduced) or diamide treatment (Oxidized). **(F)** The oxidized fraction of cytosolic eroGFP1.2 sensor under control condition. **(G)** The calculated cytosolic redox potential is approximal −328 mV. Scale bars, 10 μm. Unpaired one-tailed Student's *t*-test was used for E. **, $P < 0.01$; ****, $P < 0.0001$.

**Table 1**
Redox potential calibration in different subcellular organelles with eroGFP1.2

| Localization | Signal peptide | Indicator | Topology | Solubility | Maximal response |
|---|---|---|---|---|---|
| Mitochondria | N-ter: Tandem Cox VIII | Mito-Tracker Red CMXRos | Matrix | Soluble | 4.82 |
| Plasma membrane | C-ter: CAAX | DiI | Membrane (Cytosol) | Membrane | 4.34 |
| Golgi apparatus | N-ter: GalT4 | Golgi-Tracker Red | Lumen | Soluble | 3.87 |
| Endoplasmic reticulum | N-ter: IgH; C-ter: KDEL | ER-Tracker Red | Lumen | Soluble | 4.10 |

(Table 1). Fluorescence imaging and colocalization experiment confirmed the proper localization patterns for each construct (Fig. 4A–D).

Comparative analysis revealed significantly higher fluorescence intensity for eroGFP1.2 compared to roGFP1 in all targeted compartments (Supplementary Fig. 4A–D). Specifically, eroGFP1.2 exhibited at least a 5-fold increase in brightness in mitochondria, ER and PM. In the Golgi apparatus (Supplementary Fig. 4A, 4B and 4D), eroGFP1.2 fluorescence was approximately 2.5-fold higher than roGFP1 (Supplementary Fig. 4C).

We next performed redox calibration in each compartment using the same *in situ* titration protocol established for the cytosol (Fig. 4E and F and Supplementary Fig. 4E). The ER-localized eroGFP1.2 appeared to be almost fully oxidized (~97%), indicating a strongly oxidizing environment (−221 mV). The measured oxidation level of eroGFP1.2 in the Golgi apparatus was approximately 70%, corresponding to a redox potential of −187 mV, based on an assumed luminal pH of 6.2 consistent with the previous report [27]. It is important to note that if a neutral pH had been used in the calculation, the estimated redox potential would have been significantly different and closer to that of ER [28].

The redox status of plasma membrane is close to that of cytosol with 9.5% oxidation percentage and −324 mV. The mitochondrial matrix maintained more reduced redox state (−350 mV) than other subcellular organelles. This observation aligns well with previous findings [15,29], supporting the reliability of eroGFP1.2 for compartmental redox mapping.

Collectively, these findings demonstrate that eroGFP1.2's high signal intensity enables its effective targeting, visualization, and quantitative assessment of distinct redox potentials across multiple subcellular locations in mammalian cells.

### 2.5. *Visualization of redox changes in zebrafish tissue*

To enable *in vivo* visualization of redox changes, we co-microinjected mRNAs encoding eroGFP1.2 and HyPerRed (a red fluorescent $H_2O_2$ sensor) [30,31] into one-cell-stage zebrafish embryos (Fig. 5A). Both sensors were efficiently co-expressed (Fig. 5B and C and Supplementary Fig. 5A and 5B), and their fluorescence signals were clearly detectable in zebrafish larvae by 2 days post-fertilization (dpf). Following tailfin injury, eroGFP1.2 revealed a pronounced cytosolic oxidation at the wound margin within 25 min (Fig. 5B). Simultaneously, HyPerRed

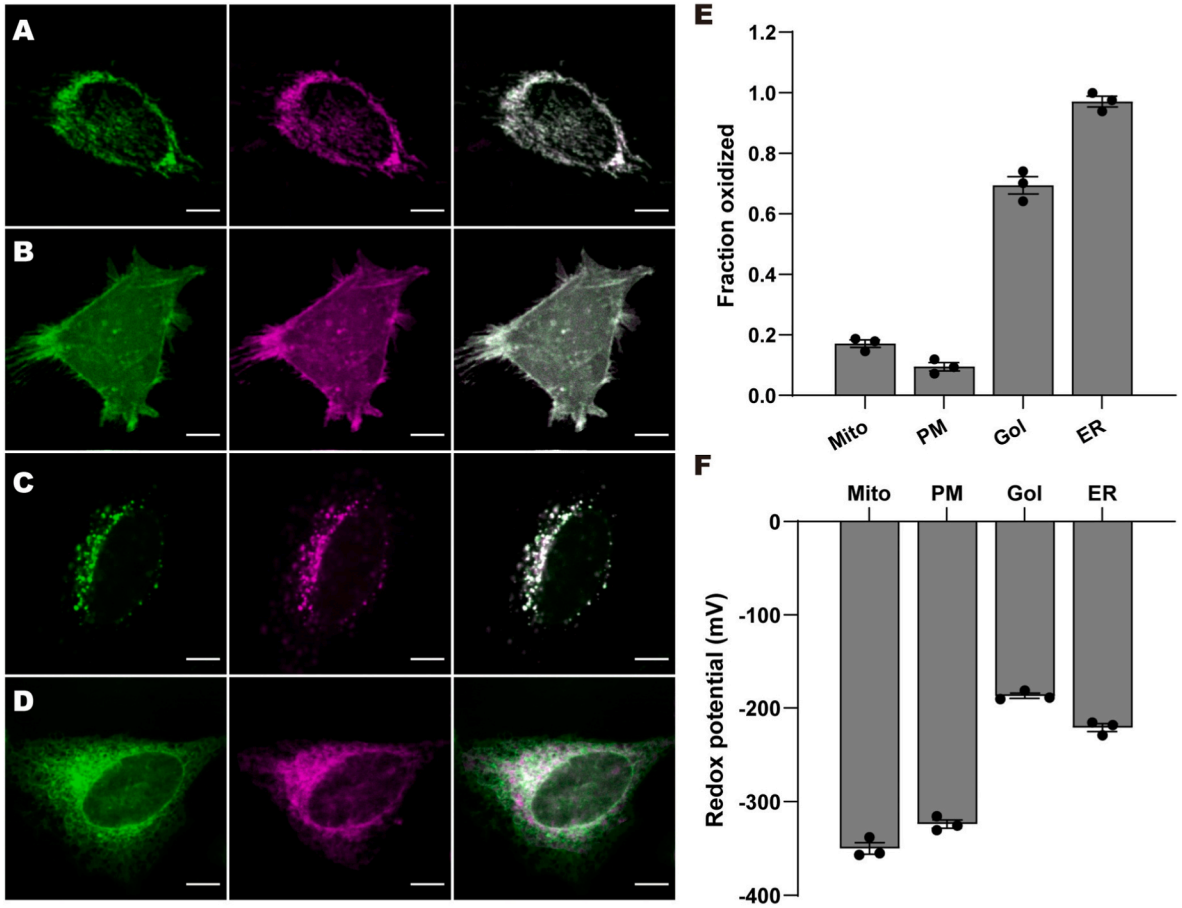


**Fig. 4. Subcellular targeting and functional calibration of the eroGFP1.2 sensor. (A–D)** Confocal microscopy images demonstrating the specific localization and functionality of eroGFP1.2 in different subcellular compartments of HeLa cells. For each compartment, the left panel shows eroGFP1.2 fluorescence (green), the middle panel shows the respective organelle-specific tracker (red; Mito-Tracker Red for mitochondria, Dil for plasma membrane, Golgi-Tracker Red for golgi apparatus, ER-Tracker Red for endoplasmic reticulum), and the right panel shows the merged image with yellow indicating co-localization. Scale bars: 10 μm. The robust co-localization confirms correct targeting. **(E)** Calculation of the oxidized fraction of the redox sensor located in different subcellular compartments of HeLa cells. The experiments were performed similarly with that of cytosolic eroGFP1.2. **(F)** Estimations of the redox poise level in four organelles of HeLa cells are detailed in the Materials and Methods section.

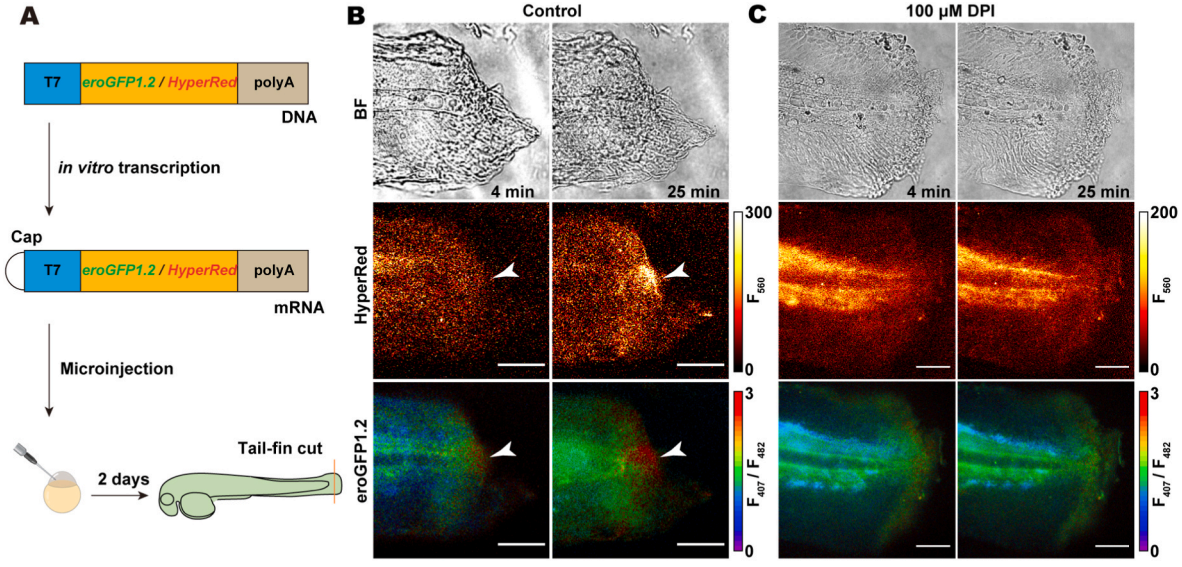


**Fig. 5.** Simultaneous visualization of redox potential and $H_2O_2$ dynamics in wound margin by co-expression of eroGFP1.2 and HyPerRed in zebrafish l**arvae. (A)** Schematic of transgenic zebrafish procedure. **(B–C)** Simultaneous visualization of redox potential and $H_2O_2$ dynamics in wound margin by co-expression of eroGFP1.2 and HyPerRed in zebrafish larvae with or without 0.1 mM DPI. Tail-fin cut was performed at the 0-min time point. Scale bars, 50 μm.

signal intensity increased significantly, showing precise spatial and temporal colocalization with the eroGFP1.2 oxidation signal (Fig. 5B).

These observations align with our previous findings that tissue wounding rapidly declines intracellular NADPH level [32], thereby promoting $H_2O_2$ generation via NADPH oxidase activity. To further validate this mechanism, we pretreated larvae with diphenyleneiodonium (DPI), a selective inhibitor of NADPH oxidases. DPI treatment completely abolished the eroGFP1.2-detected cytosolic oxidation and the HyPerRed-quantified $H_2O_2$ increase at the wound site (Fig. 5C), confirming the NADPH oxidase-dependent nature of this redox response.

Collectively, these results establish eroGFP1.2 as a robust and reliable sensor for capturing dynamic intracellular redox changes *in vivo*, particularly in the context of injury-induced oxidative signaling.

### 2.6. *Grx1-eroGFP1.2 serves as a specific sensor for glutathione redox potential*

The established Grx1-roGFP2 fusion protein enables specific live imaging of glutathione redox potential. To evaluate the glutathione specificity of the eroGFP1.2 scaffold, we generated a corresponding fusion with human Grx1 (Grx1-eroGFP1.2) and performed a comparison with Grx1-roGFP2 (Fig. 6A and Supplementary **Note 3).**

Using purified proteins, we found that oxidized Grx1-eroGFP1.2 was rapidly reduced by GSH and efficiently re-oxidized by GSSG, demonstrating its reversible responsiveness to the glutathione redox couple, similar to Grx1-roGFP2 (Fig. 6B and Supplementary Fig. 6A). In contrast, unfused eroGFP1.2 showed only subtle fluorescence response (Fig. 6B), confirming that glutathione specificity is conferred by the Grx1 moiety (Fig. 6A).

In bacterial assays, Grx1-eroGFP1.2 exhibited slightly faster $H_2O_2$ response kinetics, but a smaller dynamic range compared to Grx1-roGFP2 (Supplementary Fig. 6B–C). When expressed in HeLa cells, Grx1-eroGFP1.2 displayed significantly higher fluorescence intensity upon 407 nm excitation than Grx1-roGFP2 (Fig. 6C). Following $H_2O_2$ treatment in HeLa cells, both sensors exhibited similar response kinetics and comparable dynamic ranges (Fig. 6E, Supplementary Fig. 6D).

Taken together, these findings indicate that the Grx1-eroGFP1.2 is a reliable and specific biosensor for monitoring glutathione redox dynamics, suitable for both *in vitro* and live-cell applications.

## 3. Discussion

In this study, we developed an enhanced redox sensor, eroGFP1.2, by integrating beneficial mutations from sfGFP and pHluorin3 into the roGFP1 scaffold. This rational engineering strategy yielded a sensor with markedly improved brightness, an expanded dynamic range, and robust performance for quantitative and spatiotemporal imaging of redox dynamics in both mammalian cells and live zebrafish. The intrinsic ratiometric properties of eroGFP1.2 minimize artifacts arising from variations in sample thickness, photobleaching, or expression levels, thereby enabling robust and reliable measurements across diverse biological contexts. When compared to the widely used roGFP2, eroGFP1.2 demonstrates superior fluorescence intensity at 400 nm excitation, comparable intensity at 480 nm, reduced pH sensitivity, and a larger redox-dependent signal change at 480 nm, making it a better alternative for redox potential detection for both one- and two-photon microscopy.

Despite advances in redox sensor design over the past decade, the fluorescence intensity and response range of roGFPs remain critical constraints [33,34], limiting applications in whole organisms and challenging subcellular compartments like golgi apparatus. While

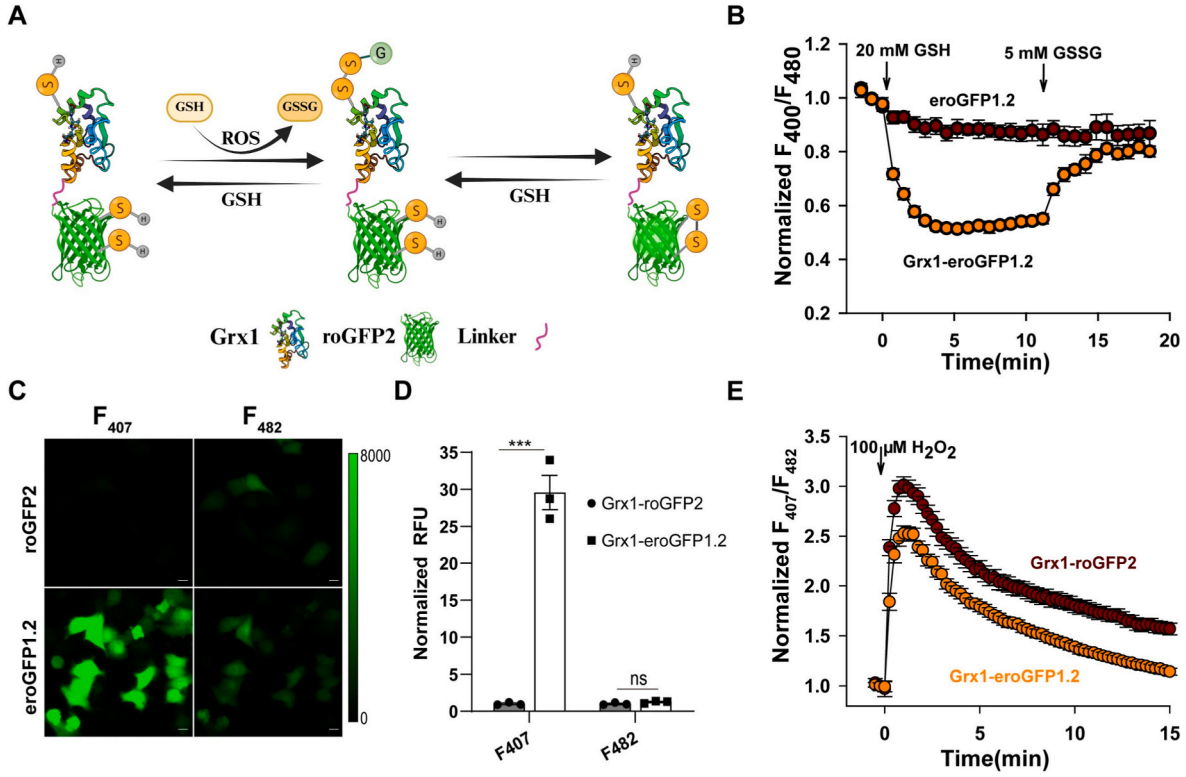


**Fig. 6. Grx1-eroGFP1.2 facilitates the specific detection of glutathione. (A)** Schematic illustration of the working model for Grx1-eroGFP1.2 (Created in BioRender. Ma, Z. (2026) https://BioRender.com/sxijwh5). **(B)** Oxidized forms of Grx1-eroGFP1.2, eroGFP1.2 were treated with 20 mM GSH to initiate reduction, followed by reoxidation with 5 mM GSSG after 10 min. The incomplete reduction of Grx1-roGFP2 by GSH is attributable to trace GSSG. **(C–D)** Representative fluorescence images (C) and quantitative analysis (D) of HeLa cells expressing Grx1-roGFP2 and Grx1-eroGFP1.2. Scale bar: 10 μm. **(E)** Fluorescence response trajectories of HeLa cells expressing Grx1-roGFP2 or Grx1-eroGFP1.2 upon treatment with 0.1 mM $H_2O_2$. Unpaired one-tailed Student's *t*-test was used for E. ns*, $P < 0.01$; ****, $P < 0.0001$.

eroGFP1.2 achieves hyper-fluorescence in the ER, mitochondria, and plasma membrane, its signal in the Golgi apparatus remains suboptimal. To address this, future iterations could incorporate folding-enhancing mutations from advanced GFP variants, such as extra-Superfolder GFP and mGreenLantern [35,36], to improve stability and brightness in these environments. Furthermore, although eroGFP1.2 accurately reports the highly oxidized baseline of the ER (~100% oxidized in resting HeLa cells), its saturation in this compartment precludes monitoring further oxidative shifts. For ER-specific applications, integrating design principles from specialized sensors like roGFP-iL [37] or roGFP-iX [38], which exhibit shifted redox sensitivity, into the eroGFP1.2 scaffold could yield an optimized ER sensor with enhanced dynamic range and signal fidelity. Another critical consideration for redox calibration is the pH of different subcellular organelles. Accurate pH measurement is essential for correct redox potential calculation, as an incorrect assumption (e.g., using a neutral pH for the acidic Golgi lumen) can lead to a significant artifact [27]. This is particularly important for calibrating sensor in other acidic compartments, such as various endosomes within the exocytosis pathway.

The practical utility of eroGFP1.2 was confirmed by visualizing cytosolic oxidation dynamics during the wound response in zebrafish. This highlights the sensor's potential for *in vivo* applications. We anticipate that eroGFP1.2 and its derivatives will be valuable tools for investigating redox dynamics within specific subcellular organelles during diverse physiological and pathological processes, such as cell protrusion formation [39].

Beyond its use as a stand-alone cytosolic sensor, the enhanced brightness of eroGFP1.2 makes it an ideal scaffold for targeted biosensors. We demonstrated that fusion with Grx1 confers specificity for the glutathione redox couple. It would be interesting to explore fusions with other redox-active proteins, such as orp1 [40] and tsa2 for hydrogen peroxide [41], Thioredoxin-1 (Trx1) for Trx1 redox state [42], which could generate novel sensors illuminating specific redox couples or oxidant species. This strategy would significantly expand the toolkit for dissecting redox poise and its regulatory mechanisms.

Our rational design strategy, leveraging mutations from bright, stable GFPs, demonstrates broad applicability across redox sensor optimization. For instance, we successfully applied this approach to engineer eroGFP2.2 (this study), which exhibits enhanced brightness analogous to eroGFP1.2. Similarly, the incorporation of sfGFP mutations into roGFPs resulted in the creation of sfroGFP2 [43] and an endoplasmic reticulum-specific sensor, ERroGFP-S4 [44], further demonstrating the broad applicability of this approach. Moreover, this optimization strategy has been applied for cpFP-based sensors, such as iATPSnFR [45] and GRIT [46] sensors. Thus, we expect this strategy to be applicable for optimizing other GFP-based sensors [18,20,47], and cpFP-based sensors [32,47].

In summary, we have engineered a bright, sensitive redox-sensitive GFP variant, eroGFP1.2. Experimental validation confirms its efficacy as a powerful tool for investigating compartment-specific redox potential *in vitro* and *in vivo*. We believe this rational design approach, leveraging mutations from optimized fluorescent proteins, provides a streamlined and effective strategy for accelerating the development of biosensors targeting previously challenging or unelucidated metabolites and cellular processes.

## 4. Materials and Methods

### 4.1. Rational design and plasmids construction

To generate a property enhanced roGFP sensor, we have introduced L220F, M153T, F46L alterations and Superfolder mutation sites (S30R/S39R/N105T/Y145F/I171V/A206V) into roGFP1. All variants were constructed via inverse PCR using Prime Star DNA polymerase on *pRSETb* vector. For cytosolic expression in HeLa cells, the cDNA encoded eroGFP1.2 was digested with *BamHI* and *HindIII* and ligated to *pcDNA3.1(+)*. To express eroGFPs in mitochondrial matrix, a duplex mitochondrial signal peptide of cytochrome *c* oxidase subunit VIII was fused at the N-terminus. Other plasmids harboring specific subcellular signals were obtained from Addgene, and we directly replaced initial genes with the eroGFP sensor (Table 1).

### 4.2. Protein expression and purification

The constructed plasmids were expressed in *Escherichia coli* BL21 (DE3) and induced by 1 mM isopropyl-β-thiogalactopyranoside (IPTG). The recombinant protein was purified by nickel affinity chromatography (GE healthcare) following the manufacturer's protocol. In brief, cell pellets were re-suspended in binding buffer (100 mM sodium phosphate, 500 mM sodium chloride, and 50 mM imidazole, pH 7.4) and sonicated for 10 min. The cell free lysate was centrifuged at 9000 g for 30 min and applied to a pre-equilibrated Ni-NTA column, followed by washing the column with binding buffer and eluted with the buffer containing 300 mM imidazole. The purified proteins were concentrated by filtration (Centricon 10; Amicon) and desalted (Sephadex G25, GE Healthcare) into a standard HEPES buffer (100 mM HEPES, 100 mM sodium chloride; pH 7.4).

### 4.3. Fluorescence property measurement in vitro and in bacteria

Fluorescence spectra were collected on a Cary Eclipse spectrofluorimeter (Varian) at 37 °C. Samples consisted of 1 μM sensor in buffer with 10 mM DTT and 0.1 mM diamide to obtain reduced and oxidized status, respectively. For redox titration, probes were diluted in degassed HEPES buffer containing 1 μM protein and 10 mM DTT (mixture of oxidized and reduced forms, varied from 0:10 to 10:0 in 1 mM increments) as redox buffers and incubated at 30 °C for 1 h before measuring fluorescence excitation intensity. The thermal stability of redox sensors was performed by denaturation with a thermos cycler (Biometra, Germany) at 60-90 °C for 30 min and the brightness of denatured sample was immediately collected with the microplate reader. The specific fluorescence responses of the Grx1-fused sensors to glutathione were evaluated by first treating the purified, oxidized proteins with 20 mM GSH for 11 min, followed by the addition of 5 mM GSSG for 8 min.

The optical density of bacteria expressed roGFP was diluted to 0.05 with HEPES buffer and fluorescence (excitation at 400 nm and 485 nm, emission at 528 nm) was measured in three replications. Response kinetic of indicators in *E. coli* cells suspension was monitored by addition 10 mM DTT and 0.5 mM diamide for 30 min. The response of bacteria expressing Grx1-roGFP sensors to hydrogen peroxide was assessed by adding 0.1 mM $H_2O_2$ (Sigma-Aldrich) to the cell suspension and monitoring the fluorescence traces for 20 min.

$F_{400}$ and $F_{485}$ are defined as the emission fluorescence intensity captured under excitation at 400 nm and 485 nm, respectively. The ratiometric signal $R_{400/485}$ is defined as the ratio of emission fluorescence intensity under two excitation lights at 400 nm and 485 nm ($F_{400}/F_{485}$). The dynamic range was calculated using the maximal excitation ratio under oxidation state (Rox) divided to the minimal excitation ratio under reduction state (Rred).

### 4.4. Western blot

For Western blot analysis, bacterial cultures of equal optical density (OD600) were harvested by centrifugation and lysed directly in 1 × SDS sample buffer supplemented with 1 mM PMSF (Beyotime Biotechnology). Total protein lysates (10 μg per lane) were separated by sodium dodecyl sulfate-polyacrylamide gel electrophoresis (SDS-PAGE) and subsequently transferred onto PVDF membranes via electroblotting. The membranes were then blocked and probed with the following primary antibodies: anti-His (Proteintech, Cat No. 66005-1-Ig; 1:5000) and anti-RpoB (Solarbio, Cat No. K013257RR). After incubation with horseradish

peroxidase (HRP)-conjugated secondary antibodies, protein bands were visualized using a chemiluminescence detection mixture (Roche) and imaged.

### 4.5. Cell culture and imaging

HeLa cells were maintained in Dulbecco's modified Eagle's medium (DMEM, hyclone) supplemented with 10% FBS (Gibco). Cells were digested and counted, then 40,000 cells were plated on a 4-well glass bottom dish (35 $mm^2$) per well. The plasmids coding eroGFP1.2 were transfected using lipofectamine 2000 (Invitrogen) as the manual description. About 24 h after transfection, cells were subjected to imaging in HBSS buffer (10 mM HEPES, 140 mM NaCl, 5 mM KCl, 4 mM $NaHCO_3$, 0.45 mM $KH_2PO_4$, 0.35 mM $NaHPO_4$, 1 mM $CaCl_2$, 0.5 mM $MgSO_4$, 10 mM D-Glucose, pH 7.4). Wide-field observations were performed on a Nikon Eclipse Ti-E automatic microscope (Nikon Instruments) with a PlanApo VC60, 1.20 numerical aperture (NA), water-immersion objective (Nikon). Filters used for dual-excitation ratio imaging of eroGFP1.2 were purchased from Semrock: an 407/17 excitation filter, an 482/30 excitation filter, and one emission filters 535/40. The two excitation filters were alternated by Lambda 10-XL filter wheel (Shutter Instruments). Images were captured using 1280 × 1024 format, 12 bit depth. We created pseudocolored images by dividing the 407 nm excitation image by the 480 nm excitation image of the same cell using ImageJ software.

To measure the fluorescence response of the roGFP sensors, HeLa cells expressing the sensors were treated with either 0.1 mM diamide or 10 mM DTT. The fluorescence changes were recorded immediately following treatment. To specifically assess the kinetics of the Grx1-eroGFP1.2 sensor in response to hydrogen peroxide, 0.1 mM $H_2O_2$ was added to the cell culture medium, and fluorescence was monitored for 15 min.

To confirm the correct subcellular targeting of the roGFP sensors, HeLa cells expressing the sensors were co-stained with commercially available organelle markers (Beyotime), following the manufacturer's instructions. In brief, Mito-Tracker Red CMXRos (Cat No. C1049B, 0.2 μM) for mitochondria, DiI (Cat No. C1036, 6 μM) for the plasma membrane, Golgi-Tracker Red (Cat No. C1043, 450 μM) for the Golgi apparatus, and ER-Tracker Red (Cat No. C1041S, 0.33 μM) for the endoplasmic reticulum. The roGFP signal (green) was excited with a 488 nm laser and its emission was collected through a 500-550 nm bandpass filter. The organelle markers (red) were excited with a 561 nm laser, and the emission was collected through a 570-50 nm bandpass filter.

### 4.6. Intracellular redox potential calibration with eroGFP1.2 sensor

The calculations of the intracellular redox potential are described as previously reported [15,27,29]. In brief, the first step is to calculate the oxidized to reduced fraction. The ratio of the oxidized to reduced forms of the sensor was determined ratiometrically from the fluorescence intensities obtained at two excitation wavelengths (400 nm and 480 nm), correcting for the background. The fraction oxidized (F) was calculated using Equation (1):

$$F = (R - R_{red}) \ / \ (R_{ox} - R_{red}) \quad \text{(Eq. 1)}$$

Where R is the measured fluorescence ratio (F400/F480) of the sample, Rred is the ratio for the fully reduced state, and Rox is the ratio for the fully oxidized state.

The apparent redox potential (E) for the intracellular roGFP sensor was subsequently calculated using the Nernst equation as Equation (2):

$$E = E_0' - (RT / 2F) \times \ln((1 - R_{ox}) / R_{ox}) \quad \text{(Eq. 2)}$$

Here, $E_0$ represents the midpoint potential of the specific roGFP sensor, which was determined experimentally by calibrating the sensor *in situ* with the reduced DTT and the oxidized DTT. R is the gas constant (8.315 J $K^{-1}$ $mol^{-1}$), T is the absolute temperature (303.15 K), n is the number of transferred electrons (2), and F is the Faraday constant ($9.649 \times 10^4$ C $mol^{-1}$).

Redox potential depends intrinsically on pH. The pH dependence of the midpoint potential can be calculated as Equation (3).

$$E_0^{pH} = E_0' - 60.1 \times (pH - 7) \quad \text{(Eq. 3)}$$

### 4.7. In vitro transcription

The coding sequences of the enhanced redox-sensitive green fluorescent protein (*eroGFP1.2*) and the red hydrogen peroxide sensor (*HyPerRed*) subcloned into the pTol2 vector backbone, which includes a T7 promoter and an SV40 polyadenylation signal. Following PCR amplification, capped mRNA was synthesized *in vitro* using the mMESSAGE mMACHINE kit (Qiagen), following the manufacturer's instructions. Residual DNA templates were digested with 2 units of DNase I, and mRNA was purified by precipitation with lithium chloride at −20 °C for 2 h.

### 4.8. Zebrafish husbandry and in vivo imaging

Zebrafish (*Danio rerio*) were maintained according to established protocols under standard laboratory conditions. All animal procedures were conducted in compliance with ethical regulations and were approved by the Institutional Animal Care and Use Committee of Xiamen University.

For dual imaging of $H_2O_2$ and redox dynamics, *eroGFP1.2* and *HyPerRed* mRNAs were mixed at equal concentrations (final concentration: 50 ng/μl each). One nanoliter of the mixture was injected into one-cell-stage zebrafish embryos. Injected embryos were cultured at 28 °C in egg water supplemented with 0.2 mM N-phenylthiourea (PTU; Sigma) to inhibit melanogenesis and ensure optical transparency. Embryos were raised under standard light/dark cycles for 2 days prior to imaging experiments. At 2 days post-fertilization (dpf), larvae were anesthetized in E3 medium (5 mM NaCl, 0.17 mM KCl, 0.33 mM $CaCl_2$, 0.33 mM $MgSO_4$, 0.6 mM Tricaine). Tail-fin tip amputation was performed under a stereomicroscope using a scalpel or microsurgical blade. Post-injury, larvae were embedded in 1% low-melting-point agarose in glass-bottomed dishes for subsequent imaging.

To assess the contribution of NADPH oxidase to ROS generation, larvae were pretreated with 0.1 mM diphenyleneiodonium (DPI; Sigma) for 30 min in E3 medium prior to tail-fin injury, as previously reported. Live imaging was conducted using a fluorescence microscope equipped with a Plan Apo 20 × /0.75 NA objective. The following excitation/emission filter sets were used: eroGFP1.2: Excitation: 407/17 nm or 482/35 nm; Emission: 535/40 nm; HyPerRed: Excitation: 560/40 nm; Emission: 630/60 nm.

Image processing and quantitative analysis were performed using standardized methods as described previously. All settings were kept constant throughout imaging sessions to ensure consistency across experimental conditions.

### 4.9. Statistics & reproducibility

Two-way ANOVA was used for paired comparisons. Paired or unpaired Student's *t*-test was used for group comparisons. No statistical method was used to predetermine sample size. For all experiments, the replicates are biological from independent experimental units or subjects. For all data, error bars or shaded regions indicate the SEM. For statistical analysis, *, $P < 0.05$; **, $P < 0.01$; ***, $P < 0.001$; ****, $P < 0.0001$. All statistical analyses and graphical representations were performed using Graphpad Prim (V9.5.1) or Sigmaplot12.5. The figures were compiled and finalized using Adobe Illustrator 2020. The schematic graphs were created using BioRender(Graphical Abstract, Created

in BioRender. Ma, Z. (2026) https://BioRender.com/slsqvkv).

## CRediT authorship contribution statement

**Zhengcai Ma:** Conceptualization, Funding acquisition, Methodology. **Jianbin Cao:** Funding acquisition, Methodology. **Hongxiang Zeng:** Investigation, Methodology. **Jiahuan Zhu:** Data curation, Formal analysis, Investigation, Methodology. **Runchun Li:** Data curation. **Xueling Wang:** Formal analysis. **Cun Yin:** Investigation. **Lingyang Chen:** Investigation. **Bing Liu:** Writing – review & editing. **Rong Shen:** Writing – review & editing. **Mingcang Wang:** Funding acquisition. **Wengang Li:** Resources. **Jingxun Wu:** Methodology, Resources. **Dan Du:** Methodology, Resources. **Rongkun Tao:** Project administration, Resources, Supervision, Writing – original draft, Writing – review & editing.

## Declaration of competing interest

Z.M, R.T, J.C, and J.Z have submitted a patent application to the Chinese patent office pertaining to the development and application aspect of eroGFP1.2 in this work. The remaining authors declare no competing interests.

## Acknowledgments

We appreciate the technical assistance and kind support from Tian-Lun Chen and Hanyang Hu. This work was supported by National Science and Technology Innovation 2030 Major Program of the Ministry of Science and Technology (2021ZD0202203 to R.T), National Natural Science Foundation of China (32171090 to R.T), Fujian Science and Technology Commission (2026R11040124 to R.T), Xiamen University President's Fund (20720250186 to R.T); The 2026 Gansu Provincial Colleges and Universities Young Doctors "Entering Enterprises and Parks" Project (2026QB-102; to Z.M), 2026 Gansu Provincial College and University Industry Support Program Project (2026CYZC-066; to Z.M), The 2021 Project for Enhancing the Innovation Capacity of Higher Education Institutions of Gansu Provincial Department of Education (No. 2021A-152; to Z.M), the 2019 Project for Enhancing the Innovation Capacity of Higher Education Institutions of Gansu Provincial Department of Education (No. 2019A-127; to Z.M), and the Medical Science and Technology Project of Zhejiang Province (2024KY1827、2024KY525 to J. C; 2024KY521 to M.W), Taizhou Science and Technology Project (23ywa48 to J. C), and the National Natural Science Foundation of China (82372788 to D. D).

## Appendix A. Supplementary data

Supplementary data to this article can be found online at https://doi.org/10.1016/j.redox.2026.104147.

## Data availability

All data supporting the findings of this study are available either within the article and its supplementary information files or from the corresponding authors upon reasonable request. Requests will be processed and fulfilled within four weeks. Relevant plasmids generated in this study are available upon request, and signature of a Material Transfer Agreement between the Xiamen University and the requestor.

## References

[1] S.J. Forrester, et al., Reactive oxygen species in metabolic and inflammatory signaling, Circ. Res. 122 (2018) 877–902. https://doi.org/10.1161/circresaha.117.311401.
[2] D.P. Jones, Redox sensing: orthogonal control in cell cycle and apoptosis signalling, J. Intern. Med. 268 (2010) 432–448. https://doi.org/10.1111/j.1365-2796.2010.02268.x.
[3] M. Rojkind, et al., Role of hydrogen peroxide and oxidative stress in healing responses, Cell. Mol. Life Sci. 59 (2002) 1872–1891. https://doi.org/10.1007/pl00012511.
[4] C. Lindermayr, A. Yildirim, Redox-signaling in innate immune memory: similar mechanisms in animals/humans and plants, Redox Biol. 84 (2025) 103702. https://doi.org/10.1016/j.redox.2025.103702.
[5] M.A. Rahman, et al., Recent advances in cellular signaling interplay between redox metabolism and autophagy modulation in cancer: an overview of molecular mechanisms and therapeutic interventions, Antioxidants 12 (2023). https://doi.org/10.3390/antiox12020428.
[6] S. Mani, et al., Therapeutic targeting of mitochondrial plasticity and redox control to overcome cancer chemoresistance, Antioxidants Redox Signal. 39 (2023) 591–619. https://doi.org/10.1089/ars.2023.0379.
[7] A.A. Hasan, et al., The thioredoxin system of mammalian cells and its modulators, Biomedicines 10 (2022). https://doi.org/10.3390/biomedicines10071757.
[8] C.G. Miller, et al., NADPH-dependent and -independent disulfide reductase systems, Free Radic. Biol. Med. 127 (2018) 248–261. https://doi.org/10.1016/j.freeradbiomed.2018.03.051.
[9] C. Landeta, et al., Disulfide bond formation in prokaryotes, Nat. Microbiol. 3 (2018) 270–280. https://doi.org/10.1038/s41564-017-0106-2.
[10] A. Ayer, et al., Distinct redox regulation in sub-cellular compartments in response to various stress conditions in Saccharomyces cerevisiae, PLoS One 8 (2013) e65240. https://doi.org/10.1371/journal.pone.0065240.
[11] L.P. Roma, J.C. Jonas, Nutrient metabolism, subcellular redox state, and oxidative stress in pancreatic islets and β-Cells, J. Mol. Biol. 432 (2020) 1461–1493. https://doi.org/10.1016/j.jmb.2019.10.012.
[12] D.P. Jones, Y.M. Go, Redox compartmentalization and cellular stress, Diabetes Obes. Metabol. 12 (Suppl 2) (2010) 116–125. https://doi.org/10.1111/j.1463-1326.2010.01266.x.
[13] X. Liu, et al., RoGFP1 is a quantitative biosensor in maize cells for cellular redox changes caused by environmental and endogenous stimuli, Biochem. Biophys. Res. Commun. 452 (2014) 503–508. https://doi.org/10.1016/j.bbrc.2014.08.107.
[14] C.T. Dooley, et al., Imaging dynamic redox changes in mammalian cells with green fluorescent protein indicators, J. Biol. Chem. 279 (2004) 22284–22293. https://doi.org/10.1074/jbc.M312847200.
[15] G.T. Hanson, et al., Investigating mitochondrial redox potential with redox-sensitive green fluorescent protein indicators, J. Biol. Chem. 279 (2004) 13044–13053. https://doi.org/10.1074/jbc.M312846200.
[16] J.D. Pédelacq, et al., Engineering and characterization of a Superfolder green fluorescent protein, Nat. Biotechnol. 24 (2006) 79–88. https://doi.org/10.1038/nbt1172.
[17] H. Gu, et al., Nonionotropic action of an acid-sensing ion channel inhibits leukemogenesis in the acidic bone marrow niche, J. Clin. Investig. 135 (2025). https://doi.org/10.1172/jci189051.
[18] H. Katayama, et al., A sensitive and quantitative technique for detecting autophagic events based on lysosomal delivery, Chem. Biol. 18 (2011) 1042–1052. https://doi.org/10.1016/j.chembiol.2011.05.013.
[19] C. Zhou, et al., Monitoring autophagic flux by an improved tandem fluorescent-tagged LC3 (mTagRFP-mWasabi-LC3) reveals that high-dose rapamycin impairs autophagic flux in cancer cells, Autophagy 8 (2012) 1215–1226. https://doi.org/10.4161/auto.20284.
[20] M.J. Mahon, pHluorin2: an enhanced, ratiometric, pH-sensitive green florescent protein, Adv. Biosci. Biotechnol. 2 (2011) 132–137. https://doi.org/10.4236/abb.2011.23021.
[21] G. Miesenböck, et al., Visualizing secretion and synaptic transmission with pH-sensitive green fluorescent proteins, Nature 394 (1998) 192–195. https://doi.org/10.1038/28190.
[22] J.M. Jacobsen, et al., Housing mice near vs. below thermoneutrality affects drug-induced weight loss but does not improve prediction of efficacy in humans, Cell Rep. 43 (2024) 114501. https://doi.org/10.1016/j.celrep.2024.114501.
[23] A.H. Andreassen, et al., Evolution of warming tolerance alters physiology and life history traits in zebrafish, Nat. Clim. Change 15 (2025) 665–672. https://doi.org/10.1038/s41558-025-02332-y.
[24] S.I. Fukushima, et al., Extremely sensitive genetically encoded temperature indicator enabling measurement at the organelle level, ACS Sens. 9 (2024) 3889–3897. https://doi.org/10.1021/acssensors.3c02658.
[25] Y. Fan, H.W. Ai, Development of redox-sensitive red fluorescent proteins for imaging redox dynamics in cellular compartments, Anal. Bioanal. Chem. 408 (2016) 2901–2911. https://doi.org/10.1007/s00216-015-9280-3.
[26] C. Wang, et al., Development of a genetically encoded sensor for arginine, ACS Sens. 10 (2025) 1260–1269. https://doi.org/10.1021/acssensors.4c03174.
[27] C. Miró-Vinyals, et al., Characterization of the glutathione redox state in the Golgi apparatus, Redox Biol. 81 (2025) 103560. https://doi.org/10.1016/j.redox.2025.103560.
[28] J. Birk, et al., Endoplasmic reticulum: reduced and oxidized glutathione revisited, J. Cell Sci. 126 (2013) 1604–1617. https://doi.org/10.1242/jcs.117218.
[29] M. Gutscher, et al., Real-time imaging of the intracellular glutathione redox potential, Nat. Methods 5 (2008) 553–559. https://doi.org/10.1038/nmeth.1212.
[30] A.I. Kostyuk, et al., Hypocrates is a genetically encoded fluorescent biosensor for (pseudo)hypohalous acids and their derivatives, Nat. Commun. 13 (2022) 171. https://doi.org/10.1038/s41467-021-27796-2.
[31] V.V. Belousov, et al., Genetically encoded fluorescent indicator for intracellular hydrogen peroxide, Nat. Methods 3 (2006) 281–286. https://doi.org/10.1038/nmeth866.

[32] R. Tao, et al., Genetically encoded fluorescent sensors reveal dynamic regulation of NADPH metabolism, Nat. Methods 14 (2017) 720–728. https://doi.org/10.1038/nmeth.4306.
[33] D.S. Bilan, V.V. Belousov, New tools for redox biology: from imaging to manipulation, Free Radic. Biol. Med. 109 (2017) 167–188. https://doi.org/10.1016/j.freeradbiomed.2016.12.004.
[34] A. Chandrasekharan, et al., A high-throughput real-time in vitro assay using mitochondrial targeted roGFP for screening of drugs targeting mitochondria, Redox Biol. 20 (2019) 379–389. https://doi.org/10.1016/j.redox.2018.10.013.
[35] J.Y. Choi, et al., The mechanism of folding robustness revealed by the crystal structure of extra-superfolder GFP, FEBS Lett. 591 (2017) 442–447. https://doi.org/10.1002/1873-3468.12534.
[36] B.C. Campbell, et al., mGreenLantern: a bright monomeric fluorescent protein with rapid expression and cell filling properties for neuronal imaging, Proc. Natl. Acad. Sci. USA 117 (2020) 30710–30721. https://doi.org/10.1073/pnas.2000942117.
[37] I. Aller, et al., Development of roGFP2-derived redox probes for measurement of the glutathione redox potential in the cytosol of severely glutathione-deficient rml1 seedlings, Front. Plant Sci. 4 (2013) 506. https://doi.org/10.3389/fpls.2013.00506.
[38] J.R. Lohman, S.J. Remington, Development of a family of redox-sensitive green fluorescent protein indicators for use in relatively oxidizing subcellular environments, Biochemistry 47 (2008) 8678–8688. https://doi.org/10.1021/bi800498g.
[39] V.V. Pak, et al., Ultrasensitive genetically encoded indicator for hydrogen peroxide identifies roles for the oxidant in cell migration and mitochondrial function, Cell Metab. 31 (2020) 642–653.e646. https://doi.org/10.1016/j.cmet.2020.02.003.
[40] M. Gutscher, et al., Proximity-based protein thiol oxidation by H2O2-scavenging peroxidases, J. Biol. Chem. 284 (2009) 31532–31540. https://doi.org/10.1074/jbc.M109.059246.
[41] B. Morgan, et al., Real-time monitoring of basal H2O2 levels with peroxiredoxin-based probes, Nat. Chem. Biol. 12 (2016) 437–443. https://doi.org/10.1038/nchembio.2067.
[42] Y. Fan, et al., Monitoring thioredoxin redox with a genetically encoded red fluorescent biosensor, Nat. Chem. Biol. 13 (2017) 1045–1052. https://doi.org/10.1038/nchembio.2417.
[43] K.C. Heimsch, et al., Structure and function of redox-sensitive superfolder green fluorescent protein variant, Antioxidants Redox Signal. 37 (2022) 1–18. https://doi.org/10.1089/ars.2021.0234.
[44] J. Hoseki, et al., Development of a stable ERroGFP variant suitable for monitoring redox dynamics in the ER, Biosci. Rep. 36 (2016). https://doi.org/10.1042/bsr20160027.
[45] M.A. Lobas, et al., A genetically encoded single-wavelength sensor for imaging cytosolic and cell surface ATP, Nat. Commun. 10 (2019) 711. https://doi.org/10.1038/s41467-019-08441-5.
[46] R. Tao, et al., A genetically encoded ratiometric indicator for tryptophan, Cell Discov. 9 (2023) 106. https://doi.org/10.1038/s41421-023-00608-1.
[47] R. Tao, et al., Multicoloured fluorescent indicators for live-cell and in vivo imaging of inorganic mercury dynamics, Free Radic. Biol. Med. 121 (2018) 26–37. https://doi.org/10.1016/j.freeradbiomed.2018.04.562.